# Geochemistry, Geophysics, Geosystems®

## RESEARCH ARTICLE

**Key Points:**

- A shallow, very strong negative $V_p$ anomaly imaged under the explosive, submarine Kolumbo volcano, Greece, using full-waveform inversion
- The high-fidelity image and petrologic data indicate the anomaly is a small (∼0.6-km wide, ∼2-km deep), magma chamber with ∼42% of melt
- The chamber was missed by travel-time tomography indicating similar reservoirs may have gone undetected at other volcanoes

**Supporting Information:**

Supporting Information may be found in the online version of this article.

**Correspondence to:**

K. Chrapkiewicz and M. Paulatto,
k.chrapkiewicz17@imperial.ac.uk;
m.paulatto@imperial.ac.uk

# Magma Chamber Detected Beneath an Arc Volcano With Full-Waveform Inversion of Active-Source Seismic Data

K. Chrapkiewicz[1], M. Paulatto[1], B. A. Heath[2,3], E. E. E. Hooft[2], P. Nomikou[4], C. B. Papazachos[5], F. Schmid[6,7], D. R. Toomey[2], M. R. Warner[1], and J. V. Morgan[1]

[1]Department of Earth Science and Engineering, Imperial College London, London, UK, [2]Department of Earth Sciences, University of Oregon, Eugene, OR, USA, [3]Now at National Tsunami Warning Center, Palmer, AK, USA, [4]Department of Geology and Geo-Environment, National and Kapodistrian University of Athens, Athens, Greece, [5]Geophysical Laboratory, Aristotle University of Thessaloniki, Thessaloniki, Greece, [6]GEOMAR Helmholtz-Centre for Ocean Research, Kiel, Germany, [7]Now at K.U.M., Umwelt- und Meerestechnik Kiel GmbH, Kiel, Germany

**Abstract** Arc volcanoes are underlain by complex systems of molten-rock reservoirs ranging from melt-poor mush zones to melt-rich magma chambers. Petrological and satellite data indicate that eruptible magma chambers form in the topmost few kilometres of the crust. However, very few chambers have ever been definitively located, suggesting that most are too short-lived or too small to be imaged, which has direct implications for hazard assessment and modeling of magma differentiation. Here we use a high-resolution technology based on inverting full seismic waveforms to image a small, high-melt-fraction magma chamber that was not detected with standard seismic tomography. The melt reservoir extends from ∼2 to at least 4 km below sea level (b.s.l.) at Kolumbo—a submarine volcano near Santorini, Greece. The chamber coincides with the termination point of the recent earthquake swarms and may be a missing link between a deeper melt reservoir and the high-temperature hydrothermal system venting at the crater floor. The chamber poses a serious hazard as it could produce a highly explosive, tsunamigenic eruption in the near future. Our results suggest that similar reservoirs (relatively small but high-melt-fraction) may have gone undetected at other active volcanoes, challenging the existing eruption forecasts and reactive-flow models of magma differentiation.

**Plain Language Summary** Arc volcanoes, which mark the curved boundaries between converging tectonic plates, host the most explosive events on Earth. The associated hazard depends on how much mobile magma is currently present shallow beneath a volcano. Standard tomographic methods used so far have relatively low resolution and give a blurred picture of only the largest molten-rock bodies. In particular, they struggle to distinguish between mobile magma and melt spread between tightly packed mineral grains. This study, a first in volcanology, combines a next-generation tomographic method with extraordinarily dense seafloor recordings of controlled marine sound sources. This state-of-the-art experiment at Kolumbo volcano, offshore of Santorini allowed us to detect a body of mobile magma which has been growing at an average rate of $4 \times 10^6$ m$^3$ per year since the last eruption in 1650 CE. This rate is large enough to counteract the effect of cooling and crystallization. Our results show that Kolumbo poses a serious threat and deserves a real-time monitoring facility. Despite the excellent data coverage, the small magma body was missed by standard tomography. This suggests that applying next-generation imaging methods to already-well-studied volcanoes may lead to similar discoveries. We envision that small-volume, high-melt-fraction reservoirs may be more widespread than previously thought.

## 1. Introduction

Arc volcanoes are the surface expression of magmatic processes that originate from the partial melting of the mantle above subducting plates (England & Katz, 2010). The thermodynamic conditions encountered by the melt as it moves toward the surface govern the volcanic eruption style (Cashman et al., 2017). Highly explosive eruptions of evolved, volatile-rich, viscous magmas at volcanic arcs (Bachmann & Bergantz, 2009) account for ∼95% of human fatalities associated with eruptive phenomena (Brown et al., 2017). The explosivity is enhanced at (semi-)submerged volcanoes due to magma-water interactions (Peckover et al., 1973; Wohletz & Heiken, 1992). Such events can lead to high and voluminous ash clouds, tsunami, and extensive pumice rafts, as occurred in the 1600 BC Santorini (Bond & Sparks, 1976), 1650 AD Kolumbo (Cantner et al., 2014; Fuller et al., 2018), and the recent Tonga (Kusky, 2022; Kubota et al., 2022) eruptions.

The plumbing systems of arc volcanoes comprise a vertically extensive network of melt reservoirs (Cashman et al., 2017). A step change from melt-controlled to crystal-controlled rheology naturally divides these reservoirs into (melt-rich) magma chambers and (melt-poor) mush zones (Sparks et al., 2019). It is widely accepted that magma differentiation occurs primarily in the deep crust (Annen et al., 2006), while shallow melt storage conditions control the style and volume of eruptions (Cashman et al., 2013; Popa et al., 2021). The question of whether a shallow reservoir is a magma chamber or a mush zone is critical for assessing eruption likelihood and dynamics. Presence of mobile melt (magma) allows for a rapid eruption (Caricchi et al., 2021; Seropian et al., 2021), while pre-eruptive crystallinity affects buoyancy-driven outgassing (Parmigiani et al., 2017). Just as important for hazard assessment is the reservoir geometry. The spatial distribution of melt can be used to estimate the magma recharge rate and the likely volume of future eruptions.

### 1.1. Need for High-Resolution Imaging of Volcanoes

While petrology gives invaluable insights into thermal evolution and ascent history of magma (e.g., Druitt et al., 2012), constraining reservoir geometry and current storage conditions under active volcanoes requires geophysical imaging. Seismic tomography has provided strong evidence for partial melting beneath many active volcanoes and has helped constrain magma storage depths and volumes (e.g., Heath et al., 2015; Kiser et al., 2018; McVey et al., 2020; Paulatto et al., 2012; Ward et al., 2014). The seismological evidence is broadly consistent with low melt fraction storage (Lees, 2007), but the inherent resolution limits (Malcolm & Trampert, 2011; Paulatto et al., 2022) lead to significant over- and under-estimation of a reservoir's volume and melt fraction, respectively. Although the evidence for crystal mush reservoirs seems compelling, the picture is far from complete. It is unclear whether magma can be rapidly extracted from crystal mush and directly erupted or whether it must first accumulate in high melt fraction magma chambers or lenses (Sparks et al., 2019). The question of how eruptible magma can be extracted from mush reservoirs is also hotly debated (Holness et al., 2019). Persistent melt lenses may have been overlooked if they are smaller than the resolution limits of the geophysical methods used to date. Such "covert" melt lenses have been drilled at ~2 km b.s.l. at several volcanoes (Rooyakkers et al., 2021). Although their prevalence is unknown, they may pose a significant hazard, affecting the availability of eruptible magma.

Traditional seismic imaging methods are unsuitable for addressing these questions since they lack the resolution required to detect melt lenses. We show that full-waveform inversion (FWI) can overcome this limitation and can provide robust constraints on melt fraction. FWI is well-suited for detecting crustal magma (Morgan et al., 2013), but requires dense sources and/or receivers. Focusing on a submarine volcano has the advantage of dense marine seismic acquisition. Our method can achieve a resolution of a few hundred metres, enough to detect small melt lenses that have so far remained beyond reach (Morgan et al., 2013).

### 1.2. Kolumbo Volcano

Here, we use full-waveform seismic imaging to study Kolumbo, an active submarine volcano located in the Santorini volcanic field (SVF), along the Hellenic Arc (Figure 1a). Kolumbo is the most active center of seismic (Andinisari et al., 2021; Bohnhoff et al., 2006; Dimitriadis et al., 2009; Schmid et al., 2022) and high-temperature hydrothermal activity within the SVF (Carey et al., 2013; Hübscher et al., 2006; Kilias et al., 2013; Rizzo et al., 2016; Sigurdsson et al., 2006). It last erupted in 1650 AD in a highly explosive, tsunamigenic event (Ulvrova et al., 2016) which produced a few km$^3$ of hydrous, biotite-rich rhyolitic lava (Cantner et al., 2014; Konstantinou, 2020). Despite the high heat and gas fluxes (Rizzo et al., 2019) which suggest an elevated magmatic activity, little is known about the underlying magmatic system. Local-earthquake tomography showed a 5%-reduction in $S$-wave velocity at 5–7 km b.s.l. (Dimitriadis et al., 2010). Its interpretation as a magma chamber was utilized in petrological (Cantner et al., 2014) and numerical studies (Konstantinou, 2020). Active-source travel time tomography does not detect a significant anomaly in the uppermost 6 km (McVey et al., 2020), with just a reduction of 3% in $P$-wave velocity at 2–4 km b.s.l. directly below the edifice (Hooft et al., 2019).
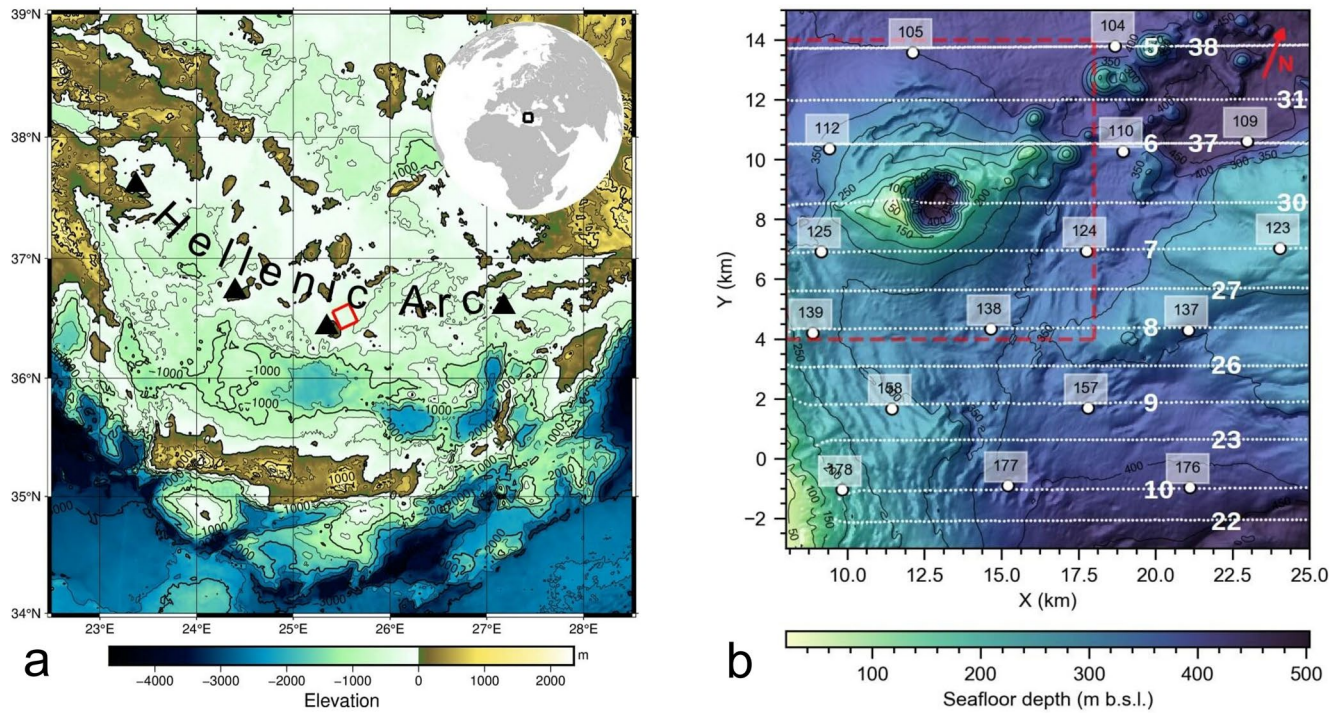
**Figure 1.** Study area and data-acquisition geometry. (a) Regional topography around the Hellenic arc; black triangles denote active volcanic centers—from W to E: Methana, Milos, Santorini and Nisyros. (b) Acquisition geometry in local coordinates annotated white circles—ocean-bottom seismometers and their IDs; white dots— airgun shots; white numbers—shot-line IDs (note, some lines were shot twice); red square—zoomed area shown in Figure 3.

## 2. Data and Methods

### 2.1. Data Selection and Processing

We apply 3D acoustic isotropic FWI (Morgan et al., 2013; Tarantola, 1984) to a wide-angle, multi-azimuth seismic data set (Hooft et al., 2017) consisting of early arriving waves generated by densely spaced airgun shots and recorded by ocean-bottom seismometers (Figure 1b). The analyzed data set is a subset of the data collected in the PROTEUS experiment (Hooft et al., 2017) contained in a $17 \times 18$ km wide box (Figure 1b), comprising 16 ocean bottom seismometers (OBSs) and 1,505 air-gun shots fired at ∼150 m intervals along the profile lines.

The local Cartesian coordinate system was obtained by rotating a local E-N coordinate system centered at 25.3971°E 36.4042°N by 25.5 counterclockwise. Traces where direct water waves interfere with the crustal refractions (shot-receiver offset less than 5 km) were excluded from the data set, followed by manual removal of bad-quality traces, resulting in an average of 977 traces per OBS. Each trace was 5-s long, sampled at 2.5 ms. The data were filtered with a minimum-phase, frequency-domain, band-pass Butterworth filter of corner frequencies 2–3–4.5–6.5 Hz followed by muting before, and 1 s after, first breaks calculated from the starting model (see below).

### 2.2. Full-Waveform Inversion

We used an explicit, time-domain, least-squares-optimized, finite-difference solver of the acoustic, isotropic, 3D wave equation implemented in the FULLWAVE3D package (Warner et al., 2013) with effective accuracy of sixth order in space and fourth order in time. As the number of air-gun shots was much greater than the number of OBSs, source-receiver reciprocity was used by labeling sources as receivers and receivers as sources.

Our starting P-wave velocity model was derived by first-arrival travel-time tomography (Heath et al., 2019) and discretized at 50-m interval in all dimensions. The density was calculated at each iteration from that model using an empirical relation (Gardner et al., 1974), except for a constant value in the water. The seabed was modeled implicitly as a velocity contrast. The sea surface was simulated as a flat, planar free surface located one node

above the top of the model grid. Absorbing boundaries (Cerjan et al., 1985) of 2.5-km width were used elsewhere. A single-source wavelet assigned to all shots was extracted from the data by deghosting stacked, high-quality, near-offset traces using an initial-guess wavelet and a Wiener filter.

A least squares misfit between synthetic and field data, both normalized by their respective norms, was minimized with a steepest-descent algorithm preconditioned by an approximation of the diagonal Hessian of the misfit function (Warner et al., 2013). Both the misfit gradient and the step-length were calculated using the adjoint method (Lions, 1972; Tarantola, 1984). The regularization involved smoothing the misfit gradient by a Gaussian filter over two (local wavelengths) horizontally and one vertically. Both the source wavelet and field data were low-pass filtered at a cut-off frequency increasing by 0.5 Hz from 3 (the lowest inverted frequency) to 6.5 Hz across eight blocks of 20 iterations, totaling 160 iterations.

The gradient-based FWI algorithms based on the least squares misfit, such as the one used here, require a starting model that is good enough to match the majority of observed data to a half of the lowest inverted frequency (Hole et al., 2005). When this condition is not met, the prevailing "cycle-skipped" data may drive the inversion toward a wrong local minimum (Virieux & Operto, 2009). This means that travel-time data inverted for the starting model to be used in FWI needs to be obtained with a well-sampled seismic survey. The data behind our starting model was collected with the same dense geometry that was used for FWI. The high quality of the starting model was confirmed by reproducing most of the observed waveforms in the offset-range of interest down to a half the cycle at the lowest inverted frequency. This frequency was chosen to be 3 Hz based on the trade-off between the poor S/N ratio at lower frequencies and the worse accuracy of the model at higher frequencies (>4 Hz).

The main result of this study is a *P*-wave velocity model of the subsurface at and around Kolumbo. The model is constrained to a $17 \times 18$ km horizontal domain (Figure 1b) and stretches down to 4 km below sea level, sampled regularly at a 50-m interval. Synthetic waveforms calculated through this model match the observed data much better than for the starting model and the inversion converged to a waveform-misfit minimum (Figure 2, Figures S6–S17 in Supporting Information S1).

### 2.3. Resolution and Uncertainty Analysis

We analyzed phase spectra (wrapped between $-\pi$ and $\pi$ radians) of the early synthetic and observed arrivals in order to estimate the S/N ratio of the field data and the adequacy of the input and forward modeling (Shah et al., 2012). Phase-residual plots of early synthetic and observed arrivals were used to assess the quality of the starting model, in particular, to detect problems with data cycle-skipping indicated by abrupt changes from $-\pi$ to $\pi$ (or vice versa) between neighboring stations (Figure 2).

To assess the effective resolving power of the inversion, in particular, to quantify the expected underestimation of velocity anomalies, we performed a suite of spike tests (Rawlinson & Spakman, 2016). We used the same strategy and input as for the field-data inversion. The only difference was replacing the observed data with acoustic synthetics calculated through an ensemble of 12 models constructed by perturbing the starting model with a suite of spherically symmetric 3D Gaussian anomalies centered roughly at the observed low-velocity anomaly (13.25; 8.75; 2.75 km), with full widths at half-maximum of 0.2, 0.8, and 1.4 km and peak amplitudes equal to 1%, 5%, 10% and 50% of the background model. Only anomalies stronger than 10% were detectable. The best recovery (80% of the true peak amplitude) was obtained for the 50% anomaly of 0.8-km width (Figure S5 in Supporting Information S1). Anomalies smaller and/or weaker were not recovered. Larger (1.4 km) but weaker (10%) anomalies yielded worse recovery than the best case, while the 50% anomaly of 1.4-km width led to artifacts characteristic of cycle-skipping.

To detect potential outliers in the OBS data and quantify the uncertainty of the final model we used jack-knife resampling (e.g., Rawlinson et al., 2014). We performed 16 field-data inversions, every time excluding a different OBS from the data set. The standard deviation of the models recovered after 160 iterations (Figure S4 in Supporting Information S1) was taken as a proxy for uncertainty.

### 2.4. Effective-Medium Calculation

We used the self-consistent scheme (Berryman, 1980) to calculate the effective bulk and shear moduli of a two-phase, partially molten granite with a composition that is the average of seven rock samples from the most
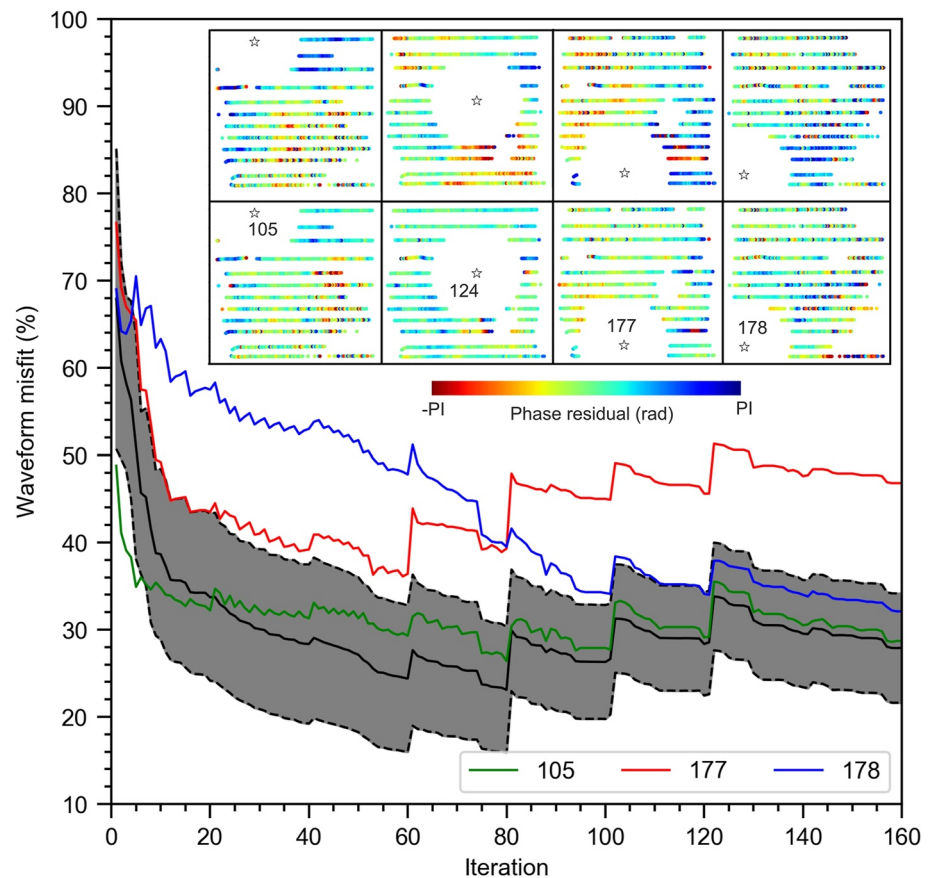
**Figure 2.** Data-misfit across iterations. (a) Objective function defined as $L^2$-norm misfit of normalized waveforms, averaged over ocean bottom seismometers (OBSs), shown as a black line between 1 gray bounds; stations 177 and 178 with the largest misfit, along with a more typical station 105, are highlighted in color; inset: phase residual of four OBSs (annotated stars) at 3 Hz for starting (top) and final (bottom) model. (b) Observed versus synthetic waveforms at OBS 105, line 27 for starting (top) and final (bottom) model; reduction velocity on the vertical axis is 5 km/s.

recent Kolumbo eruption (supplement of Klaver et al., 2016). For the solid phase, we used $v_P = (6.25 \pm 0.13)$ km/s, $v_S = (3.67 \pm 0.12)$ km/s, and $\rho = (2660 \pm 20)$ kg/m$^3$ from the laboratory measurements at 200 MPa and 30°C of more than 100 granite samples (Christensen & Stanley, 2003). We corrected the velocities (Christensen, 1979) for lithostatic pressure (66 MPa) and a solidus temperature of 700°C (Boettcher & Wyllie, 1968), obtaining $v_P = 6.20$ km/s and $v_S = 3.58$ km/s. Thus, the temperature effect is a second-order factor and partial melting is required to explain the observed velocity anomaly. For the fluid phase, we use $\rho = 2{,}110$ kg/m$^3$ and bulk modulus $K = 8.08$ GPa from the thermodynamic model based on the Birch-Murnaghan equation (Ueki & Iwamori, 2016). The assumption underlying the SCS calculation is spheroidal-shaped pores. We use 0.05–0.5 as the range of plausible aspect ratios (Takei, 2002), due to a lack of experimental constraints. We assumed the low-frequency, equilibrated limit (Biot, 1956) starting with air-filled pores followed by fluid substitution according to Gassman's equation (Gassmann, 1951). Sensitivity analysis showed that varying input parameters other than pore aspect ratio and fluid bulk modulus (which in turn is sensitive to water content) has a negligible effect on the final result.

## 3. Results

### 3.1. Kolumbo Low-Velocity Anomaly

The most striking feature of the final model is a prominent low-velocity zone (LVZ) beneath Kolumbo extending from 2.1 to at least 4 km b.s.l., with a diameter of 0.6 km for the 4 km/s contour and a minimum value of 3.4 km/s at 2.55 km b.s.l. (40% reduction relative to the starting model, see below). To highlight its geometry, we display it as a negative anomaly relative to the starting model, with the absolute values (for both the starting and
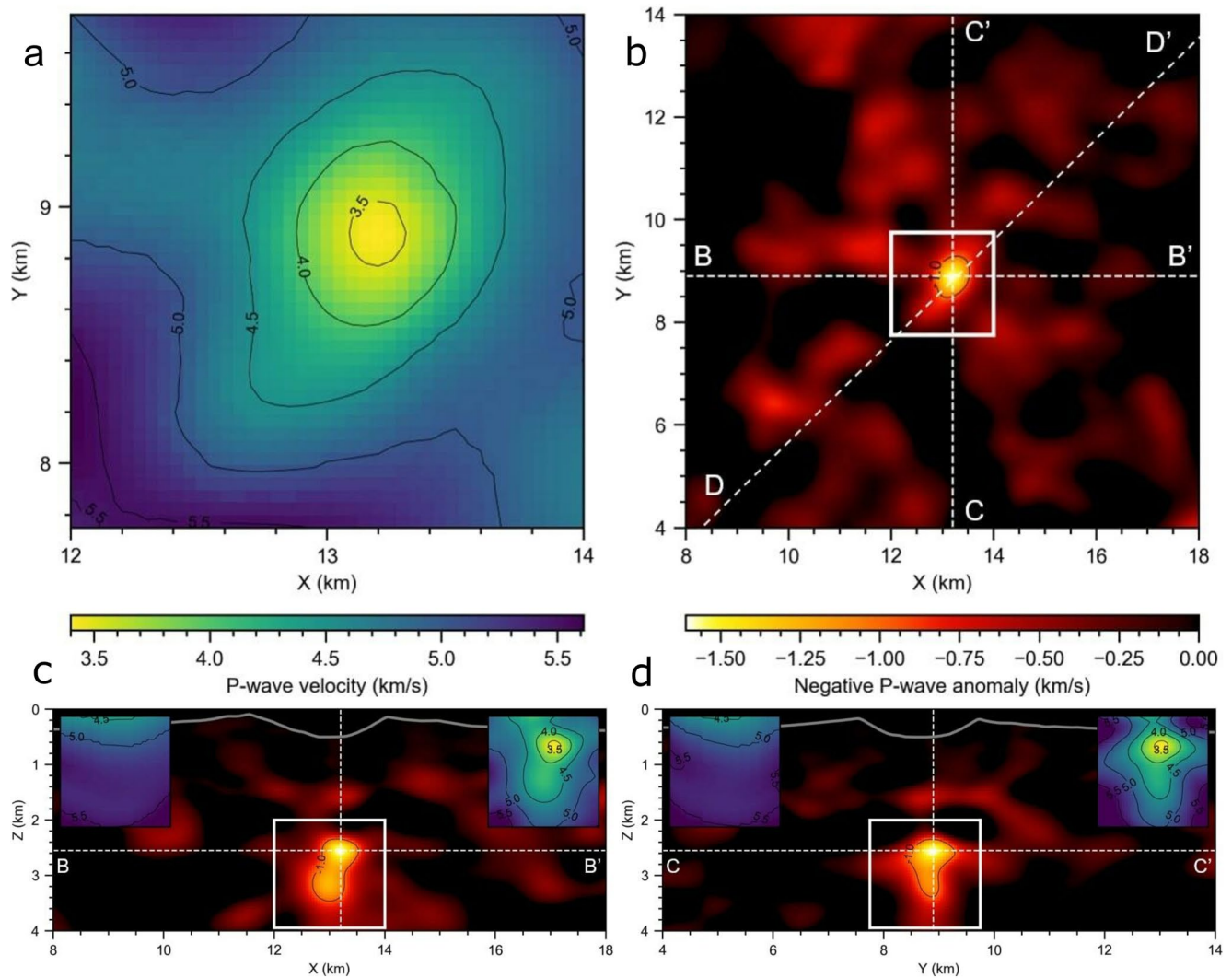
**Figure 3.** Final *P*-wave velocity model. Shown as a negative anomaly relative to the starting model. Insets: Absolute values of the starting and final model (left and right, respectively) inside the reservoir denoted by the white box. Dashed lines indicate cross-section planes.

final model) shown in the insets (Figure 3). Its shape is plume-like in the SW-NE cross-section (*Y* axis), thinner at the base where the wavelength is larger, and thus not produced by the directional smoothing which we used to regularize the inversion. The regularization leads to recovery of only 80% of the true amplitude as shown by synthetic tests (Figure S5 in Supporting Information S1). The maximum recovered anomaly was 1.6 km/s relative to the starting 5.0 km/s (Figure 3). Correcting for regularization gives approximately a 2.0 km/s anomaly (40% reduction), corresponding to a *P*-wave velocity of 3.0 km/s within the LVZ.

### 3.2. Credibility and Fidelity of the Low-Velocity Volume

Several factors make this anomaly a robust feature required by the data. First, the synthetic tests show that a similar anomaly is recoverable by our method (Figure S5 in Supporting Information S1). Second, the anomaly, although much more smeared, was already present in the high-quality starting model (Figure S1 in Supporting Information S1) obtained by travel-time tomography (Heath et al., 2019), which has lower resolution but is more robust against artifacts compared to FWI (Virieux & Operto, 2009). Third, the largest enhancement of the anomaly amplitude, corresponding to the largest improvement of waveform fit, was achieved during the first, low-frequency iterations, indicating that the anomaly is not produced by over-fitting of the high-frequency waveforms. Fourth, the feature is robust against different inversion strategies and data subsets. In particular, jack-knife
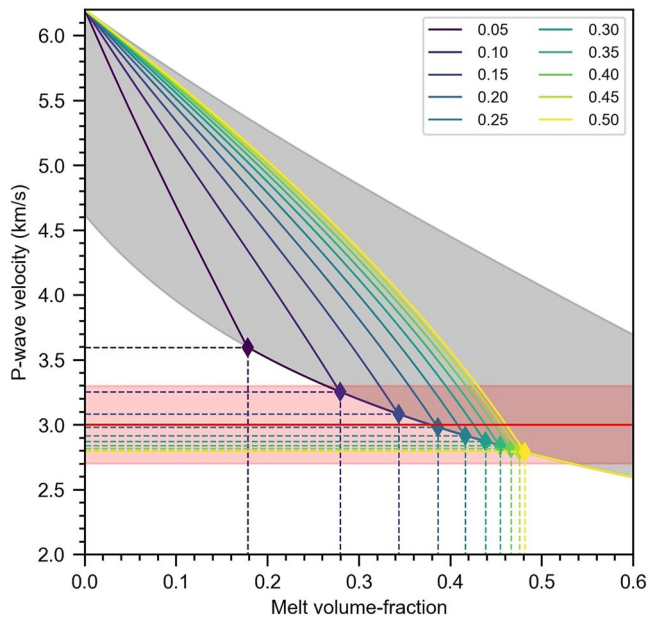
**Figure 4.** *P*-wave velocity of a granitic intrusion as a function of melt fraction. Gray area fills between the Hashin-Shtrikman bounds (Hashin & Shtrikman, 1963). Colored lines correspond to different values of the pore aspect ratio listed in the key, with rhombi marking the critical porosity (Nur et al., 1998). The maximum observed anomaly with three error bounds from jackknifing is denoted in red.

resampling shows that it is not caused by potential outliers (Figure S4 in Supporting Information S1). Although the recovered final model is likely to have errors due to data noise, inversion regularization, and the simplified physics (acoustic, isotropic, non-attenuative medium) used to calculate synthetic data, we argue that these errors are small and do not affect our conclusions (Text S2 in Supporting Information S1).

### 3.3. Melt Fraction and Melt Volume

The observed low-velocity anomaly can be explained by the presence of either melt or hydrothermal fluids (magmatic gases and/or seawater). We favor the former possibility based on independent seismic reflection observations of the hydrothermal system that place the top of the hydrothermal reservoir at ~0.6 km b.s.l. (Hübscher et al., 2006). Geochemical analysis of the hydrothermal fluids suggests that interaction of magmatic gases and seawater occurs at ~1 km b.s.l. (Rizzo et al., 2019). The hydrothermal system is not visible in our model because the shallow structure is poorly constrained by the data (see Figures S4 and S5 in Supporting Information S1). Nonetheless, the weak low-velocity layer at 1.4–1.9 km b.s.l. may be evidence of a volatile-rich lens. Although a multi-level hydrothermal system extending to the base of the observed anomaly is conceivable, the persistent seismic unrest down to 16 km b.s.l. (Schmid et al., 2022) makes this possibility less likely, as explained below.

We can also rule out the hypothesis that the LVZ is caused by a purely thermal anomaly. The temperature required to explain such a strong velocity perturbation greatly exceeds the solidus temperature for granite, implying partial melting. We interpret the LVZ as a partially molten intrusion and we assume it to be granitic (rhyolitic) based on the bulk composition of lava from the 1650 AD eruption (Cantner et al., 2014).

We estimate the maximum melt fraction of the intrusion by comparing the maximum observed *P*-wave velocity anomaly of 3.0 km/s with values calculated for partially molten granite using the self-consistent effective medium approach (Berryman, 1980), assuming melt-filled spheroidal pores (see Methods). There is a strong trade-off between the pore geometry (aspect ratio) and melt fraction. Here we assume thin, oblate pores (melt films) of aspect ratio between 0.05 and 0.5 (Takei, 2002). Recalling the uncertainty in velocity of 0.3 km/s (from jack-knifing) yields melt fractions ranging from 0.26 to 0.53 (Figure 4). Assuming the velocity error to be normally distributed (with $\sigma = 0.1$ km/s), the melt fraction is $0.42 \pm 0.04$.

The total volume of the low-velocity anomaly equals 6.2 km³, which corresponds to a sphere of 1.1 km radius. This is probably a lower bound, as the anomaly seems to extend below the bottom of the model. The total volume of melt stored in the reservoir is $(1.38 \pm 0.32)$ km³, where the error bounds come from the aspect-ratio uncertainty. Note that these values are also affected by difficult-to-quantify errors due to the simplified physics used in FWI (see e.g., Marjanović et al., 2019) and should probably be used only in comparison to other acoustic inversions.

## 4. Discussion

### 4.1. Relationship With Seismic Activity

A recent seismicity study by Schmid et al. (2022) shows that the observed anomaly coincides with the tip of a cone-shaped region hosting enhanced seismic activity in the 2006–2007 period. The earthquakes were clustered in several swarms starting with the strongest events at 6–9 depth and migrating upwards, terminating at the base of the LVZ. The swarm propagation was faster than expected for hydrothermal gases diffusing from a point source or for active diking (Schmid et al., 2022). However, the speed and focal mechanisms associated with the swarms remain consistent with melt ascent along pre-existing, subvertical pathways through a rheologically strong layer at 4–9 km b.s.l. Schmid et al. (2022) interpret this seismic activity as a result of either transport

of melt from larger depths to the observed reservoir, or formation of fractures enabling such transport which occurred after the recording period. These findings support our interpretation of a melt-filled reservoir below Kolumbo. Similar seismic activity has been recorded during several other time periods (Andinisari et al., 2021; Bohnhoff et al., 2006; Dimitriadis et al., 2009) suggests ongoing reservoir recharge by frequent injections of magma from greater depth.

### 4.2. Magma Chamber Versus Mush

The melt fraction of $0.42 \pm 0.04$ at the center of the velocity anomaly may be overestimated by neglecting the 6% of volatiles reported for the 1650 AD eruptive products (Cantner et al., 2014). However, it is likely above the critical porosity (Figure 4) corresponding to the mush-magma transition (Sparks et al., 2019), implying rheology controlled by melt rather than crystalline framework. The observed >40% reduction of *P*-wave velocity relative to the regional average is larger than for anomalies obtained by travel time tomography at other volcanoes studied to date. For example, 10% for Newberry (Heath et al., 2015), Yellowstone (Huang et al., 2015) and Mt. St. Helens (Kiser et al., 2018), 17% for Montserrat (Paulatto et al., 2019), and 21% for Santorini (McVey et al., 2020). For this reason, despite the remaining uncertainty in melt fraction, we interpret the imaged reservoir as a small magma chamber rather than a mush zone, or a hybrid reservoir in which a small magma chamber is embedded in a larger mush zone.

Petrological (Cantner et al., 2014) and numerical models (Konstantinou, 2020) of the Kolumbo magmatic system have been based on the interpretation of the low *S*-wave velocity anomaly from local-earthquake tomography (Dimitriadis et al., 2010), which is located 5–7 km b.s.l., offset from the edifice. This interpretation is inconsistent with the seismicity data (Schmid et al., 2022) which suggests that the source of melt feeding the shallow chamber may be located deeper than 9 km b.s.l., beneath a rheologically strong, seismically active layer (Schmid et al., 2022). The composition of the ascending melt is at least partially mafic, as indicated by the enclaves present in the 1650 AD lavas (Cantner et al., 2014; Klaver et al., 2016). We propose that frequent ascent of mafic melt from deeper levels leads to heating and remobilization (Burgisser & Bergantz, 2011) of the shallow felsic melt reservoir, and consequently to formation of a magma chamber.

We propose that the imaged shallow melt reservoir (Figure 5) represents the uppermost level of a multi-level system. Surprisingly, the imaged melt reservoir is not sill-like as it is elongated vertically, with a broader top. However, this shape may not be well constrained, as indicated by the relatively large uncertainty associated with this part of the model (Figure S4 in Supporting Information S1) and the smearing at the top of the recovered synthetic anomaly (Figure S5 in Supporting Information S1). If we were to treat the mushroom-like shape of the anomaly as a real feature, its broad top may represent a lens of brine (Hill et al., 2020) separated from magma ponding below the high-temperature hydrothermal system (Hübscher et al., 2015; Rizzo et al., 2016; Sigurdsson et al., 2006). In turn, the narrow base may reflect the predominant path of magma supplied through a rheologically strong layer (Schmid et al., 2022) that overlies a yet-to-be-imaged deeper mush zone. This may indicate a more complex multi-level system than numerical simulations which show small (hundreds of meters) magma chambers forming directly at the top of larger (kilometres) mush zones (Booth et al., 2019; Jackson et al., 2018).

### 4.3. Long-Term Evolution and Present State

The long-term evolution of a magma chamber depends on the time-scales of melt injection, cooling, and viscous relaxation of the surrounding crust (Degruyter & Huber, 2014). For a chamber to grow, mass injection must be faster than cooling, but slower than the viscous relaxation of elastic stress. Assuming that all of the observed melt has accumulated since the last eruption (1650 AD) and taking 2,600 $kg/m^3$ as the mafic melt density (Konstantinou, 2020), the average melt flux is equal to $4 \times 10^3$ $km^3$ $yr^{-1}$, or 330 kg/s. This is of the same order of magnitude as the estimate for nearby Santorini (Parks et al., 2012) and Montserrat (Annen et al., 2013). Calculations of eruption frequency of upper crustal silicic magma chambers using the approach of Degruyter and Huber (2014) suggest that this flux can result in tens of eruptions before mechanical lock-up, for chamber volumes of up to 20 $km^3$ and for fluxes as small as 50 kg/s (Figure 6).

The volume of mobile magma beneath Kolumbo is up to 0.02 $km^3$ (assuming a pore aspect-ratio of 0.05). This is twice the volume of magma injected in 2011–2012 beneath Santorini (Parks et al., 2012). The total volume of melt accumulated in the reservoir beneath Kolumbo ($\sim$1.4 $km^3$) is close to the $\sim$2 $km^3$ of dry-rock equivalent
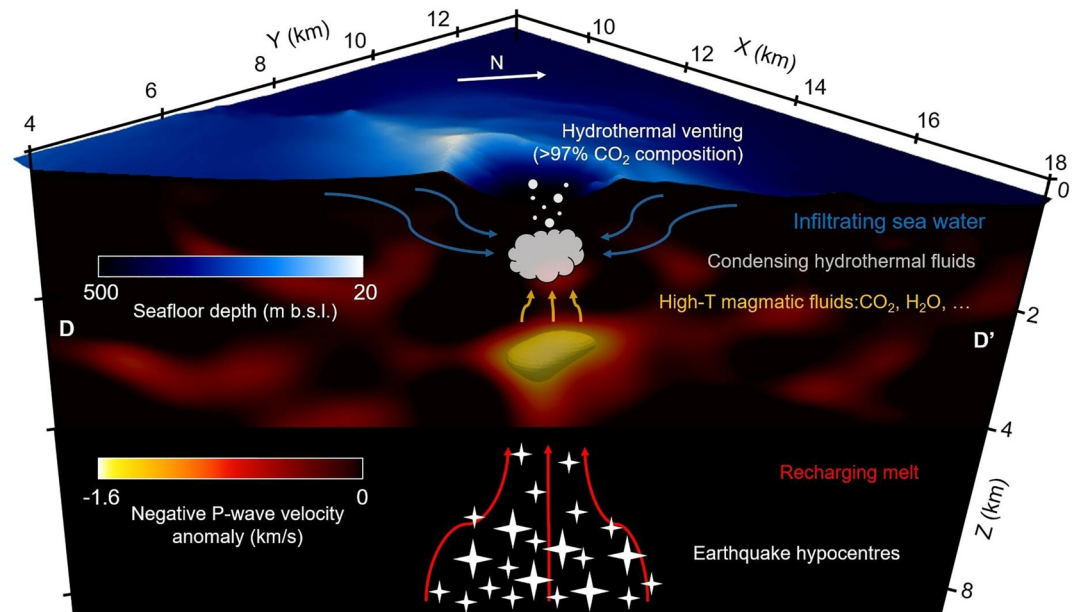
**Figure 5.** Kolumbo magmatic system. Ascending rhyolitic melt replenishes the shallow chamber. The exsolved gases mix with seawater and vent at the crater floor. The depth of hydrothermal systems is inferred from seismic reflection images (Hübscher et al., 2015) and geochemical data (Rizzo et al., 2019). The approximate earthquake locations are based on Schmid et al. (2022). The velocity anomaly is extracted from the final model along the DD' profile (Figure 3b). No vertical exaggeration is applied.

(DRE) volume of the last eruption (Nomikou et al., 2014). For comparison, the DRE volume of the Mt. St. Helens 1980 eruption was 3 km$^3$ (Kiser et al., 2018). The eruption recurrence interval at Kolumbo is unknown, as only the last of five recognised eruptive phases has been dated with confidence (Nomikou et al., 2016). A sequence stratigraphic analysis indicates that all these phases occurred during the last 1.2 Ma, suggesting an average recurrence interval of ~240 ka (Preine et al., 2021). A lower bound of 10 ka was proposed based on seismic reflection data and the tectonic history of the region (Hübscher et al., 2015). While this implies a considerably longer recurrence time than the interval since Kolumbo's last eruption, a sizable lens of mobile melt ~2 km below the seafloor poses a serious threat of a highly explosive, tsunamigenic eruption in the near future. The high melt fraction implies that the reservoir could be readily mobilized by a larger influx of magma or an external trigger (Caricchi et al., 2021). The shallow reservoir depth lowers the critical overpressure needed to form and propagate a dyke to the eruptive vent (Jellinek & DePaolo, 2003). The relatively shallow water (500 m at the crater floor) is likely to enhance rather than suppress explosivity (Dürig et al., 2020). A tsunami and an eruptive column of tens of km with significant ashfall and extensive pumice rafts can be expected as the aftermath of the eruption (Kusky, 2022; Nomikou et al., 2014). Although it will probably be an order of magnitude less powerful than the recent Hunga Tonga-Hunga Ha'apai event, it may have a greater impact, considering $CO_2$ accumulated at the crater floor (Carey et al., 2013), the dense population on nearby Santorini, and the sea/air traffic in the Aegean.

## 5. Conclusions

Our study is the first application of active-source, seismic full-waveform imaging to an active volcano. High-resolution imaging combined with high-sensitivity earthquake monitoring (Schmid et al., 2022) provides unique evidence for magma transport to the shallow crust and a direct image of the resulting magma chamber beneath Kolumbo volcano. The current state of the reservoir indicates that an explosive eruption of high societal impact in the future is possible (though not imminent), thus we suggest establishing a permanent observatory involving continuous earthquake monitoring (Schmid et al., 2022) and seafloor geodesy.

Our image bridges the gap between seismic data and conceptual models of relatively small but high-melt fraction silicic bodies forming at the uppermost level of transcrustal mush systems. Remarkably, the chamber was almost entirely missed by dense travel-time tomography (Heath et al., 2019; McVey et al., 2020), which used the same
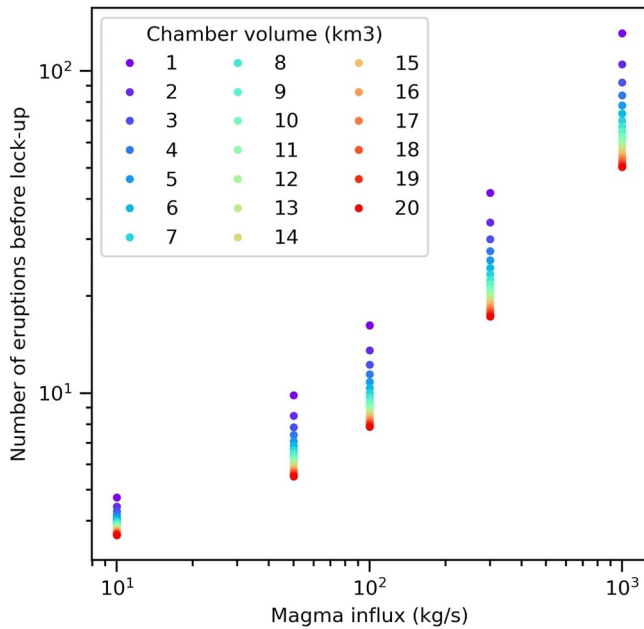
**Figure 6.** Number of eruptions from a magma chamber as a function of the melt influx and chamber volume. The relationship was calculated from the model for eruption frequency of upper crustal silicic magma chambers (Equation 45 of Degruyter & Huber, 2014), under the assumptions described therein. The model accounts for mass injection, viscous relaxation, cooling, crystallisation, gas exsolution, and eruption. The values are averages over $10^6$ Monte Carlo runs which sampled Gaussian distributions of overpressure equal to $p = (20 \pm 15)$ MPa (Konstantinou, 2020), crust viscosity equal to $\log_{10} = (20.5 \pm 1.5) \log_{10}(\text{Pa·s})$ (Konstantinou, 2020), and thermal diffusivity equal to $(3.0 \pm 0.5) 10^6$ m$^2$/s, where the uncertainties correspond to $3\sigma$ of the respective distributions. This thermal diffusivity is relatively high (Whittington et al., 2009) and was motivated by the cold upper crust and efficient heat removal via the hydrothermal system at Kolumbo.

active-source data set. Similar melt reservoirs would have gone undetected at other active volcanoes, raising the possibility that they may be more common than previously thought. Further thermomechanical modeling should give insights into the formation and longevity of such chambers.

Wider adoption of full-waveform imaging may usher a new era of volcano geophysics, increasing detectability of melt reservoirs by providing detailed images of elastic parameters, as well as more accurate background models for earthquake relocation and 3D seismic migration (Magee et al., 2018). With ever-increasing computing resources, elastic FWI (e.g., Marjanović et al., 2019) should soon be commonplace, allowing to study subaerial volcanoes as well. These targets will require modeling of irregular land surface either by using finite-element-like solvers (which require a challenging meshing step, e.g., Komatitsch & Tromp, 2002) or the augmented finite-difference method (e.g., Chrapkiewicz, 2021). Whether marine or land, elastic FWI will also require detailed a priori knowledge of the shallow subsurface and/or suppressing some of the elastic effects present in the data (e.g., Agudo et al., 2020).

Increasingly tight constraints on the spatial distribution of melt and volume of eruptible magma in the shallow crust will substantially improve our understanding of magmatic systems and revolutionize volcanic hazard assessment.

## Conflict of Interest

The authors declare no conflicts of interest relevant to this study.

## Data Availability Statement

The entire ocean bottom seismometer dataset analyzed in this study has been archived at the IRIS Data Management Center (https://doi.org/10.7914/SN/1E_2015). The FULLWAVE3D software used to invert the data can be accessed through academic collaboration with Imperial College London or a membership of the FULLWAVE consortium (Warner et al., 2013). The effective-medium properties were calculated using the ElasticC package available at http://github.com/mich-paulatto/ElasticC. The full-waveform inversion-diagnostics FullwavePy software used to QC the inversion and produce most of the figures can be downloaded from http://github.com/kmch/FullwavePy.

## References

Agudo, Ò. C., da Silva, N. V., Stronge, G., & Warner, M. (2020). Mitigating elastic effects in marine 3-D full-waveform inversion. *Geophysical Journal International*, *220*(3), 2089–2104. https://doi.org/10.1093/gji/ggz569

Andinisari, R., Konstantinou, K., & Ranjan, P. (2021). Seismicity along the Santorini-Amorgos zone and its relationship with active tectonics and fluid distribution. *Physics of the Earth and Planetary Interiors*, *312*, 106660. https://doi.org/10.1016/j.pepi.2021.106660

Annen, C., Blundy, J. D., & Sparks, R. S. (2006). The genesis of intermediate and silicic magmas in deep crustal hot zones. *Journal of Petrology*, *47*(3), 505–539. https://doi.org/10.1093/petrology/egi084

Annen, C., Paulatto, M., Sparks, R. S. J., Minshull, T. A., & Kiddle, E. J. (2013). Quantification of the intrusive magma fluxes during magma chamber growth at Soufrière Hills volcano (Montserrat, Lesser Antilles). *Journal of Petrology*, *55*(3), 529–548. https://doi.org/10.1093/petrology/egt075

Bachmann, O., & Bergantz, G. W. (2009). Rhyolites and their source mushes across tectonic settings. *Journal of Petrology*, *49*(12), 2277–2285. https://doi.org/10.1093/petrology/egn068

Berryman, J. G. (1980). Long-wavelength propagation in composite elastic media II. Ellipsoidal inclusions. *Journal of the Acoustical Society of America*, *68*(6), 1820–1831. https://doi.org/10.1121/1.385172

Biot, M. (1956). Theory of elastic waves in a fluid-saturated porous solid. 1. Low frequency range. *Journal of the Acoustical Society of America*, *28*(2), 168–178. https://doi.org/10.1121/1.1908239

Boettcher, A. L., & Wyllie, P. J. (1968). Melting of granite with excess water to 30 kilobars pressure. *The Journal of Geology*, *76*(2), 235–244. https://doi.org/10.1086/627324

Bohnhoff, M., Rische, M., Meier, T., Becker, D., Stavrakakis, G., & Harjes, H.-P. (2006). Microseismic activity in the Hellenic volcanic arc, Greece, with emphasis on the seismotectonic setting of the Santorini–Amorgos zone. *Tectonophysics*, *423*(1), 17–33. https://doi.org/10.1016/j.tecto.2006.03.024

Bond, A., & Sparks, R. S. J. (1976). The Minoan eruption of Santorini, Greece. *Journal of Geological Society of London*, *132*(1), 1–16. https://doi.org/10.1144/gsjgs.132.1.0001

Booth, C. A., Kunz, B. E., & Jackson, M. D. (2019). Heat sources and the evolution of multiple magma reservoirs in the continental crust. In *American Geophysical Union Fall Meeting 2019, abstract #V21A-03*.

Brown, S. K., Jenkins, S. F., Sparks, R. S. J., Odbert, H., & Auker, M. R. (2017). Volcanic fatalities database: Analysis of volcanic threat with distance and victim classification. *Journal of Applied Volcanology*, *6*(1), 15. https://doi.org/10.1186/s13617-017-0067-4

Burgisser, A., & Bergantz, G. W. (2011). A rapid mechanism to remobilize and homogenize highly crystalline magma bodies. *Nature*, *471*(7337), 212–217. https://doi.org/10.1038/nature09799

Cantner, K., Carey, S., & Nomikou, P. (2014). Integrated volcanologic and petrologic analysis of the 1650 AD eruption of Kolumbo submarine volcano, Greece. *Journal of Volcanology and Geothermal Research*, *269*, 28–43. https://doi.org/10.1016/j.jvolgeores.2013.10.004

Carey, S., Nomikou, P., Bell, K. C., Lilley, M., Lupton, J., Roman, C., et al. (2013). $CO_2$ degassing from hydrothermal vents at Kolumbo submarine volcano, Greece, and the accumulation of acidic crater water. *Geology*, *41*(9), 1035–1038. https://doi.org/10.1130/g34286.1

Caricchi, L., Townsend, M., Rivalta, E., & Namiki, A. (2021). The build-up and triggers of volcanic eruptions. *Nature Reviews Earth & Environment*, *2*(7), 458–476. https://doi.org/10.1038/s43017-021-00174-8

Cashman, K. V., Sparks, R. S. J., & Blundy, J. D. (2017). Vertically extensive and unstable magmatic systems: A unified view of igneous processes. *Science*, *355*(6331). https://doi.org/10.1126/science.aag3055

Cashman, K. V., Stephen, R., & Sparks, J. (2013). How volcanoes work: A 25 year perspective. *Bulletin of the Geological Society of America*, *125*(5–6), 664–690. https://doi.org/10.1130/b30720.1

Cerjan, C., Kosloff, D., Kosloff, R., & Reshef, M. (1985). A nonreflecting boundary condition for discrete acoustic and elastic wave equations. *Geophysics*, *50*(4), 705–708. https://doi.org/10.1190/1.1441945

Chrapkiewicz, K. (2021). *High-resolution imaging beneath the Santorini volcano*. PhD thesis, Imperial College London. https://doi.org/10.25560/96427

Christensen, N. I. (1979). Compressional wave velocities in rocks at high temperatures and pressures, critical thermal gradients, and crustal low-velocity zones. *Journal of Geophysical Research*, *84*(B12), 6849–6858. https://doi.org/10.1029/jb084ib12p06849

Christensen, N. I., & Stanley, D. (2003). Seismic velocities and densities of rocks. *International Geophysics*, *81*, 1587–1594.

Degruyter, W., & Huber, C. (2014). A model for eruption frequency of upper crustal silicic magma chambers. *Earth and Planetary Science Letters*, *403*, 117–130. https://doi.org/10.1016/j.epsl.2014.06.047

Dimitriadis, I., Karagianni, E., Panagiotopoulos, D., Papazachos, C., Hatzidimitriou, P., Bohnhoff, M., et al. (2009). Seismicity and active tectonics at Coloumbo reef (Aegean Sea, Greece): Monitoring an active volcano at Santorini volcanic center using a temporary seismic network. *Tectonophysics*, *465*(1–4), 136–149. https://doi.org/10.1016/j.tecto.2008.11.005

Dimitriadis, I., Papazachos, C., Panagiotopoulos, D., Hatzidimitriou, P., Bohnhoff, M., Rische, M., & Meier, T. (2010). P and S velocity structures of the Santorini-Coloumbo volcanic system (Aegean Sea, Greece) obtained by non-linear inversion of travel times and its tectonic implications. *Journal of Volcanology and Geothermal Research*, *195*(1), 13–30. https://doi.org/10.1016/j.jvolgeores.2010.05.013

Druitt, T. H., Costa, F., Deloule, E., Dungan, M., & Scaillet, B. (2012). Decadal to monthly timescales of magma transfer and reservoir growth at a caldera volcano. *Nature*, *482*(7383), 77–80. https://doi.org/10.1038/nature10706

Dürig, T., White, J. D. L., Murch, A. P., Zimanowski, B., Büttner, R., Mele, D., et al. (2020). Deep-sea eruptions boosted by induced fuel–coolant explosions. *Nature Geoscience*, *13*(7), 498–503. https://doi.org/10.1038/s41561-020-0603-4

England, P. C., & Katz, R. F. (2010). Melting above the anhydrous solidus controls the location of volcanic arcs. *Nature*, *467*(7316), 700–703. https://doi.org/10.1038/nature09417

Fuller, S., Carey, S., & Nomikou, P. (2018). Distribution of fine-grained tephra from the 1650 CE submarine eruption of Kolumbo volcano, Greece. *Journal of Volcanology and Geothermal Research*, *352*, 10–25. https://doi.org/10.1016/j.jvolgeores.2018.01.004

Gardner, G. H. F., Gardner, L. W., & Gregory, A. R. (1974). Formation velocity and density; the diagnostic basics for stratigraphic traps. *Geophysics*, *39*(6), 770–780. https://doi.org/10.1190/1.1440465

Gassmann, F. (1951). Elastic waves through a packing of spheres. *Geophysics*, *16*(4), 673–685. https://doi.org/10.1190/1.1437718

Hashin, Z., & Shtrikman, S. (1963). A variational approach to the theory of the elastic behaviour of multiphase materials. *Journal of the Mechanics and Physics of Solids*, *11*(2), 127–140. https://doi.org/10.1016/0022-5096(63)90060-7

Heath, B. A., Hooft, E. E. E., Toomey, D. R., & Bezada, M. J. (2015). Imaging the magmatic system of Newberry volcano using joint active source and teleseismic tomography. *Geochemistry, Geophysics, Geosystems*, *16*(12), 4433–4448. https://doi.org/10.1002/2015gc006129

Heath, B. A., Hooft, E. E., Toomey, D. R., Papazachos, C. B., Nomikou, P., Paulatto, M., et al. (2019). Tectonism and its relation to magmatism around Santorini volcano from upper crustal P wave velocity. *Journal of Geophysical Research: Solid Earth*, *124*(10), 10610–10629. https://doi.org/10.1029/2019jb017699

Hill, G. J., Bibby, H. M., Peacock, J., Wallin, E. L., Ogawa, Y., Caricchi, L., et al. (2020). Temporal magnetotellurics reveals mechanics of the 2012 Mount Tongariro, NZ, eruption. *Geophysical Research Letters*, *47*(8), e2019GL086429. https://doi.org/10.1029/2019gl086429

Hole, J. A., Zelt, C. A., & Pratt, R. G. (2005). Advances in controlled-source seismic imaging. *EOS Transactions*, *86*(18), 177–181. https://doi.org/10.1029/2005eo180001

Holness, M. B., Stock, M. J., & Geist, D. (2019). Magma chambers versus mush zones: Constraining the architecture of sub-volcanic plumbing systems from microstructural analysis of crystalline enclaves. *Philosophical Transactions of the Royal Society A: Mathematical, Physical & Engineering Sciences*, *377*(2139), 20180006. https://doi.org/10.1098/rsta.2018.0006

Hooft, E. E. E., Heath, B. A., Toomey, D. R., Paulatto, M., Papazachos, C. B., Nomikou, P., et al. (2019). Seismic imaging of Santorini: Subsurface constraints on caldera collapse and present-day magma recharge. *Earth and Planetary Science Letters*, *514*, 48–61. https://doi.org/10.1016/j.epsl.2019.02.033

Hooft, E. E., Nomikou, P., Toomey, D. R., Lampridou, D., Getz, C., Christopoulou, M.-E., et al. (2017). Backarc tectonism, volcanism, and mass wasting shape seafloor morphology in the Santorini-Christiana-Amorgos region of the Hellenic Volcanic Arc. *Tectonophysics*, *712*, 396–414. https://doi.org/10.1016/j.tecto.2017.06.005

Huang, H.-H., Lin, F.-C., Schmandt, B., Farrell, J., Smith, R. B., & Tsai, V. C. (2015). The Yellowstone magmatic system from the mantle plume to the upper crust. *Science*, *348*(6236), 773–776. https://doi.org/10.1126/science.aaa5648

Hübscher, C., Hensch, M., Dahm, T., Dehghani, A., Dimitriadis, I., Hort, M., & Taymaz, T. (2006). Toward a risk assessment of central Aegean volcanoes. *Eos*, *87*(39), 401. https://doi.org/10.1029/2006eo390002

Hübscher, C., Ruhnau, M., & Nomikou, P. (2015). Volcano-tectonic evolution of the polygenetic Kolumbo sub-marine volcano/Santorini (Aegean Sea). *Journal of Volcanology and Geothermal Research*, *291*, 101–111. https://doi.org/10.1016/j.jvolgeores.2014.12.020

Jackson, M. D., Blundy, J., & Sparks, R. S. J. (2018). Chemical differentiation, cold storage and remobilization of magma in the Earth's crust. *Nature*, *564*(7736), 405–409. https://doi.org/10.1038/s41586-018-0746-2

Jellinek, A. M., & DePaolo, D. J. (2003). A model for the origin of large silicic magma chambers: Precursors of caldera-forming eruptions. *Bulletin of Volcanology*, *65*(5), 363–381. https://doi.org/10.1007/s00445-003-0277-y

Kilias, S. P., Nomikou, P., Papanikolaou, D., Polymenakou, P. N., Godelitsas, A., Argyraki, A., et al. (2013). New insights into hydrothermal vent processes in the unique shallow-submarine arc-volcano, Kolumbo (Santorini), Greece. *Scientific Reports*, *3*, 1–13. https://doi.org/10.1038/srep02421

Kiser, E., Levander, A., Zelt, C., Schmandt, B., & Hansen, S. (2018). Focusing of melt near the top of the Mount St. Helens (USA) magma reservoir and its relationship to major volcanic eruptions. *Geology*, *46*(9), 775–778. https://doi.org/10.1130/g45140.1

Klaver, M., Carey, S., Nomikou, P., Smet, I., Godelitsas, A., & Vroon, P. (2016). A distinct source and differentiation history for Kolumbo submarine volcano, Santorini volcanic field, Aegean arc. *Geochemistry, Geophysics, Geosystems*, *17*(8), 3254–3273. https://doi.org/10.1002/2016gc006398

Komatitsch, D., & Tromp, J. (2002). Spectral-element simulations of global seismic wave propagation-I. Validation. *Geophysical Journal International*, *149*(2), 390–412. https://doi.org/10.1046/j.1365-246x.2002.01653.x

Konstantinou, K. I. (2020). Magma chamber evolution during the 1650 AD Kolumbo eruption provides clues about past and future volcanic activity. *Scientific Reports*, *10*, 1–12. https://doi.org/10.1038/s41598-020-71991-y

Kubota, T., Saito, T., & Nishida, K. (2022). Global fast-traveling tsunamis driven by atmospheric Lamb waves on the 2022 Tonga eruption. *Science*, *377*(6601), 91–94. https://doi.org/10.1126/science.abo4364

Kusky, T. M. (2022). Déjà vu: Might future eruptions of Hunga Tonga-Hunga Ha'apai volcano be a repeat of the devastating eruption of Santorini, Greece (1650 BC)? *Journal of Earth Sciences*, *33*(2), 229–235. https://doi.org/10.1007/s12583-022-1624-2

Lees, J. M. (2007). Seismic tomography of magmatic systems. *Journal of Volcanology and Geothermal Research*, *167*(1–4), 37–56. https://doi.org/10.1016/j.jvolgeores.2007.06.008

Lions, J. L. (1972). *Nonhomogeneous boundary value problems and applications*. Springer-Verlag.

Magee, C., Stevenson, C. T. E., Ebmeier, S. K., Keir, D., Hammond, J. O. S., Gottsmann, J. H., et al. (2018). Magma plumbing systems: A geophysical perspective. *Journal of Petrology*, *59*(6), 1217–1251. https://doi.org/10.1093/petrology/egy064

Malcolm, A. E., & Trampert, J. (2011). Tomographic errors from wave front healing: More than just a fast bias. *Geophysical Journal International*, *185*(1), 385–402. https://doi.org/10.1111/j.1365-246x.2011.04945.x

Marjanović, M., Plessix, R. E., Stopin, A., & Singh, S. C. (2019). Elastic versus acoustic 3-D full waveform inversion at the east Pacific rise 9°50′N. *Geophysical Journal International*, *216*(3), 1497–1506. https://doi.org/10.1093/gji/ggy503

McVey, B. G., Hooft, E. E., Heath, B. A., Toomey, D. R., Paulatto, M., Morgan, J. V., et al. (2020). Magma accumulation beneath Santorini volcano from P-wave tomography. *Geology*, *48*(3), 231–235. https://doi.org/10.1130/g47127.1

Morgan, J., Warner, M., Bell, R., Ashley, J., Barnes, D., Little, R., et al. (2013). Next-generation seismic experiments: Wide-angle, multi-azimuth, three-dimensional, full-waveform inversion. *Geophysical Journal International*, *195*(3), 1657–1678. https://doi.org/10.1093/gji/ggt345

Nomikou, P., Carey, S., Bell, K. L. C., Papanikolaou, D., Bejelou, K., Cantner, K., et al. (2014). Tsunami hazard risk of a future volcanic eruption of Kolumbo submarine volcano, NE of Santorini Caldera, Greece. *Natural Hazards*, *72*(3), 1375–1390. https://doi.org/10.1007/s11069-012-0405-0

Nomikou, P., Hübscher, C., Ruhnau, M., & Bejelou, K. (2016). Tectono-stratigraphic evolution through successive extensional events of the Anydros basin, hosting Kolumbo volcanic field at the Aegean Sea, Greece. *Tectonophysics*, *671*, 202–217. https://doi.org/10.1016/j.tecto.2016.01.021

Nur, A., Mavko, G., Dvorkin, J., & Galmudi, D. (1998). Critical porosity: A key to relating physical properties to porosity in rocks. *The Leading Edge*, *17*(3), 357–362. https://doi.org/10.1190/1.1437977

Parks, M. M., Biggs, J., England, P., Mather, T. A., Nomikou, P., Palamartchouk, K., et al. (2012). Evolution of Santorini volcano dominated by episodic and rapid fluxes of melt from depth. *Nature Geoscience*, *5*(10), 749–754. https://doi.org/10.1038/ngeo1562

Parmigiani, A., Degruyter, W., Leclaire, S., Huber, S., & Bachmann, O. (2017). The mechanics of shallow magma reservoir outgassing. *Journal of Geophysical Research: Solid Earth*, *119*(8), 6308–6322. https://doi.org/10.1002/2014jb011124

Paulatto, M., Annen, C., Henstock, T. J., Kiddle, E., Minshull, T. A., Sparks, R. S. J., & Voight, B. (2012). Magma chamber properties from integrated seismic tomography and thermal modeling at Montserrat. *Geochemistry, Geophysics, Geosystems*, *13*, 1–18. https://doi.org/10.1029/2011gc003892

Paulatto, M., Hooft, E. E. E., Chrapkiewicz, K., Heath, B., Toomey, D. R., & Morgan, J. V. (2022). Advances in seismic imaging of magma and crystal mush. *Frontiers in Earth Science*, *10*. https://doi.org/10.3389/feart.2022.970131

Paulatto, M., Moorkamp, M., Hautmann, S., Hooft, E., Morgan, J. V., & Sparks, R. S. J. (2019). Vertically extensive magma reservoir revealed from joint inversion and quantitative interpretation of seismic and gravity data. *Journal of Geophysical Research: Solid Earth*, *124*(11), 11170–11191. https://doi.org/10.1029/2019jb018476

Peckover, R. S., Buchanan, D. J., & Ashby, D. (1973). Fuel–coolant interactions in submarine vulcanism. *Nature*, *245*(5424), 307–308. https://doi.org/10.1038/245307a0

Popa, R.-G., Bachmann, O., & Huber, C. (2021). Explosive or effusive style of volcanic eruption determined by magma storage conditions. *Nature Geoscience*, *14*(10), 781–786. https://doi.org/10.1038/s41561-021-00827-9

Preine, J., Karstens, J., Hübscher, C., Nomikou, P., Schmid, F., Crutchley, G. J., et al. (2021). Spatio-temporal evolution of the Christiana-Santorini-Kolumbo volcanic field, Aegean Sea. *Geology*, *20*.

Rawlinson, N., & Spakman, W. (2016). On the use of sensitivity tests in seismic tomography. *Geophysical Journal International*, *205*(2), 1221–1243. https://doi.org/10.1093/gji/ggw084

Rawlinson, N., Fichtner, A., Sambridge, M., & Young, M. K. (2014). Seismic tomography and the assessment of uncertainty. In *Advances in geophysics* (Vol. 55, pp. 1–76). Elsevier.

Rizzo, A. L., Caracausi, A., Chavagnac, V., Nomikou, P., Polymenakou, P. N., Mandalakis, M., et al. (2016). Kolumbo submarine volcano (Greece): An active window into the Aegean subduction system. *Scientific Reports*, *6*, 1–9. https://doi.org/10.1038/srep28013

Rizzo, A. L., Caracausi, A., Chavagnac, V., Nomikou, P., Polymenakou, P. N., Mandalakis, M., et al. (2019). Geochemistry of $CO_2$-rich gases venting from submarine volcanism: The case of Kolumbo (Hellenic Volcanic Arc, Greece). *Frontiers in Earth Science*, *7*, 60. https://doi.org/10.3389/feart.2019.00060

Rooyakkers, S. M., Stix, J., Berlo, K., Petrelli, M., & Sigmundsson, F. (2021). Eruption risks from covert silicic magma bodies. *Geology*, *49*, 1–5. https://doi.org/10.1130/g48697.1

Schmid, F., Petersen, G., Hooft, E., Paulatto, M., Chrapkiewicz, K., Hensch, M., & Dahm, T. (2022). Heralds of future volcanism: Swarms of microseismicity beneath the submarine Kolumbo volcano indicate opening of near-vertical fractures exploited by ascending melts. *Geochemistry, Geophysics, Geosystems*, *23*(7), e2022GC010420. https://doi.org/10.1029/2022gc010420

Seropian, G., Kennedy, B. M., Walter, T. R., Ichihara, M., & Jolly, A. D. (2021). A review framework of how earthquakes trigger volcanic eruptions. *Nature Communications*, *12*(1), 1004. https://doi.org/10.1038/s41467-021-21166-8

Shah, N., Warner, M., Nangoo, T., Umpleby, A., Štekl, I., Morgan, J., & Guasch, L. (2012). Quality assured full-waveform inversion: Ensuring starting model adequacy. In *SEG technical program expanded abstracts 2012* (pp. 1–5).

Sigurdsson, H., Carey, S., Alexandri, M., Vougioukalakis, G., Croff, K., Roman, C., et al. (2006). Marine investigations of Greece's Santorini volcanic field. *Eos*, *87*(34), 337. https://doi.org/10.1029/2006eo340001

Sparks, R. S. J., Annen, C., Blundy, J. D., Cashman, K. V., Rust, A. C., & Jackson, M. D. (2019). Formation and dynamics of magma reservoirs. *Philosophical Transactions of the Royal Society A: Mathematical, Physical & Engineering Sciences*, *377*(2139), 20180019. https://doi.org/10.1098/rsta.2018.0019

Takei, Y. (2002). Effect of pore geometry on Vp/Vs: From equilibrium geometry to crack. *Journal of Geophysical Research*, *107*(B2), 2043. https://doi.org/10.1029/2001jb000522

Tarantola, A. (1984). Inversion of seismic reflection data in the acoustic approximation. *Geophysics*, *49*(8), 1259–1266. https://doi.org/10.1190/1.1441754

Ueki, K., & Iwamori, H. (2016). Density and seismic velocity of hydrous melts under crustal and upper mantle conditions. *Geochemistry, Geophysics, Geosystems*, *17*(5), 1312–1338. https://doi.org/10.1002/2015gc006242

Ulvrova, M., Paris, R., Nomikou, P., Kelfoun, K., Leibrandt, S., Tappin, D. R., & McCoy, F. W. (2016). Source of the tsunami generated by the 1650 AD eruption of Kolumbo submarine volcano (Aegean Sea, Greece). *Journal of Volcanology and Geothermal Research*, *321*, 125–139. https://doi.org/10.1016/j.jvolgeores.2016.04.034

Virieux, J., & Operto, S. (2009). An overview of full-waveform inversion in exploration geophysics. *Geophysics*, *74*(6), WCC1–WCC26. https://doi.org/10.1190/1.3238367

Ward, K. M., Zandt, G., Beck, S. L., Christensen, D. H., & McFarlin, H. (2014). Seismic imaging of the magmatic underpinnings beneath the Altiplano-Puna volcanic complex from the joint inversion of surface wave dispersion and receiver functions. *Earth and Planetary Science Letters*, *404*, 43–53. https://doi.org/10.1016/j.epsl.2014.07.022

Warner, M., Ratcliffe, A., Nangoo, T., Morgan, J., Umpleby, A., Shah, N., et al. (2013). Anisotropic 3D full-waveform inversion. *Geophysics*, *78*(2), R59–R80. https://doi.org/10.1190/geo2012-0338.1

Whittington, A. G., Hofmeister, A. M., & Nabelek, P. I. (2009). Temperature-dependent thermal diffusivity of the Earth's crust and implications for magmatism. *Nature*, *458*(7236), 319–321. https://doi.org/10.1038/nature07818

Wohletz, K., & Heiken, G. (1992). *Volcanology and geothermal energy*. University of California Press.

## References From the Supporting Information

Heath, B. A., Hooft, E. E. E., Toomey, D. R., Paulatto, M., Papazachos, C. B., Nomikou, P., & Morgan, J. V. (2021). Relationship between active faulting/fracturing and magmatism around Santorini: Seismic anisotropy from an active source tomography experiment. *Journal of Geophysical Research: Solid Earth*, *126*(8). https://doi.org/10.1029/2021jb021898

Mulder, W. A., & Plessix, R. E. (2008). Exploring some issues in acoustic full waveform inversion. *Geophysical Prospecting*, *56*(6), 827–841. https://doi.org/10.1111/j.1365-2478.2008.00708.x

Štekl, I., Umpleby, A., & Warner, M. (2010). Seismic anisotropy effects in 3D wavefield tomography. In *72nd EAGE conference & exhibition* (pp. 1–5).

Warner, M., Morgan, J., Umpleby, A., Štekl, I., & Guasch, L. (2012). Which physics for full-wavefield seismic inversion? In *74th EAGE conference & exhibition* (pp. 1–5).